ACS Partner Journal

CHEM & BIO ENGINEERING

pubs.acs.org/ChemBioEng

Article

Polythiophene-Based Nonmetal Electrocatalyst with Biocompatibility to Boost Efficient CO_2 Conversion

Xianghai Bian, Yang Ye, Sulin Ni, Bin Yang, Yang Hou, Lecheng Lei, Min Yao,* and Zhongjian Li*

Cite This: *Chem Bio Eng.* 2025, 2, 229–240

Read Online

ACCESS | Metrics & More | Article Recommendations | Supporting Information

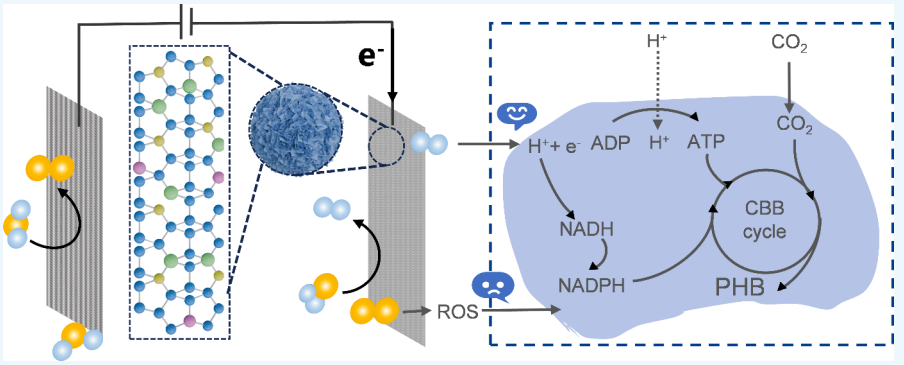

ABSTRACT: In a hybrid microbial−inorganic catalysis system, H_2 evolution reaction (HER) electrocatalysts are coupled with microorganisms to achieve the highly efficient conversion of CO_2 to value-added chemicals using H_2 as an electron mediator. However, currently developed HER electrocatalysts suffer from poor biocompatibility, hindering the performance of the system. This study presents a N- and Si-doped polythiophene nanocomposite (PTh-NSi) as a nonmetal HER electrocatalyst with biocompatibility for use in a hybrid microbial−inorganic catalysis system. By coupling PTh-NSi with *Ralstonia eutropha* H16, conversion of CO_2 to poly-β-hydroxybutyrate with a maximum yield of 662.99 ± 27.46 mg/L was achieved. The PTh-NSi electrocatalyst demonstrated HER performance in bacterial media, minimal reactive oxygen species production, and no heavy metal ion leaching, ensuring biocompatibility with *R. eutropha* H16. The interactions between PTh-NSi and *R. eutropha* H16 were revealed. This work highlights an approach to designing biocompatible catalysts for hybrid microbial−inorganic catalysis systems, offering the potential for sustainable CO_2 conversion.

KEYWORDS: *hybrid microbial−inorganic catalysis system, hydrogen evolution reaction, nonmetal electrocatalyst, biocompatibility, CO_2 reduction*

1. INTRODUCTION

The increase in atmospheric CO_2 concentration has led to significant ecological and environmental issues.[1] Thermal, photo, and electrocatalysis can enable the fixation and recycling of CO_2, but it remains challenging in converting it to C_{2+} products. In contrast, organisms can utilize enzymes to specifically convert CO_2 into multicarbon products with higher energy density and value, such as butyric acid, terpenoids, and lycopene.[2,3] Recently, decoupled microbial−inorganic catalysis systems, which spatially separate electrochemical and biochemical processes, have been developed. Liquid feedstocks from CO_2 electrocatalytic reduction of CO_2 serve as substrates for organisms to produce desirable products. However, the complexity of the equipment and difficulty in separating liquid feedstocks remain significant bottlenecks. Compared to these systems, a hybrid microbial−inorganic catalysis system, which couples microorganisms with inorganic catalysis in a single reactor, offers a more efficient solution.[4,5]

Microbial conversion of CO_2 requires reducing the equivalents. Therefore, electron transfer from electrodes to microorganisms in the hybrid microbial−inorganic catalysis system is essential. For microorganisms that cannot undergo direct electron transfer through physical contact with solid electrodes, an electron carrier is required to facilitate indirect electron transfer. Hydrogen is a utilizable electron carrier for microorganisms due to its low molecular weight and high diffuse rate through cell membranes. Additionally, hydrogen provides microorganisms with energy for reproduction, metabolism, and synthesis of products.[6] In hybrid catalysis

Received: October 4, 2024
Revised: January 5, 2025
Accepted: January 6, 2025
Published: January 13, 2025

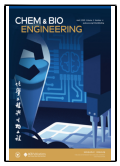

systems, hydrogen is generated at the cathode by water electrolysis and then utilized *in situ* by microorganisms. Therefore, efficient hydrogen evolution reaction (HER) electrocatalysts are crucial. Although metal-based HER catalysts exhibit excellent performance, the leaching of metal ions can inhibit microorganism activities.[7,8] In recent years, carbon-based HER catalysts, typically formed by doping the heterostructure with metals, have been developed.[9,10] These metallic active sites will leach low concentrations of metal ions during aqueous reactions, which can be toxic to coupled bacteria. For example, Ni^{2+} and Co^{2+} ions at concentrations as low as 25 μmol/L can cause significant toxicity to bacteria.[11]

Given these considerations, nonmetal carbon-based catalysts that completely eliminate metal leaching are more biocompatible for hybrid microbial−inorganic catalysis systems. Besides biocompatibility, the high activity of the catalyst is also crucial. When combined with biological systems, the HER catalyst must exhibit excellent hydrogen production performance under neutral conditions and in complex solution environments (coexisting with inorganic salts, proteins, and extracellular polymeric substances secreted by microorganisms). Furthermore, the long growth cycles of microorganisms (~10 days) require excellent stability of the accompanying HER catalyst. Therefore, designing biocompatible HER catalysts involves higher requirements and more challenges compared to traditional HER catalyst design.

Previous studies on nonmetal electrocatalysts focused on the formation of graphene structures through heat treatments or the addition of graphene in the raw material. A graphitic network would enhance the electron and electrolyte transports as well as the electrochemical performance. However, due to the chemical inertness of the graphene, there was limited synergy between it and other doping components. Electrically conductive polymers (ECPs) provide a conductive energy band structure due to their $\pi-\pi$ conjugated properties and are widely used as biocompatible anode materials for microbial fuel cells.[12−14] Polythiophene (PTh) is one such ECP that exhibits stable properties. The charge distribution in PTh is not uniform with more negative charges on the S atoms which strengthens the C−S bond to improve stability.[15] Meanwhile, highly efficient catalysis was achieved by transferring electrons using the very high nucleophilicity of C−S. These characteristics give PTh the potential to meet the requirements of stability and biocompatibility. To improve catalytic activity, modification of PTh by doping heteroatoms (N, S, P, B, Si, etc.) is a feasible method.[16] Heteroatom-doping can induce charge transferring between carbon and heteroatoms, optimizing the adsorption/desorption of reactants and intermediates at active sites for higher catalytic performance. In particular, N-doping is becoming a trend for introducing heteroatoms. The electronegativity of N (3.04) is greater than that of C (2.55), and its atomic radius is slightly smaller than that of C. Doping with pyridine N, pyrrole N, graphite N, etc., can achieve electronic polarization and enhance the adsorption capacity of the active center for H atoms, resulting in excellent HER performance.[17,18] Moreover, N-doping has been widely reported to improve biocompatibility by providing sites for microorganism adhesion through increased electrode roughness.[19,20] However, the hydrophobic surface of PTh hinders the adsorption and activation of water molecules, which is the first step of HER.[21,22] Especially in the hybrid catalysis system, where a neutral electrolyte (pH = 6.8−7.4) is required, the lack of protons adds to the difficulty of the activation step. Therefore, Si was selected to improve the hydrophilic properties of PTh due to its good hydrophilicity and ease of compounding with other materials.[23] Additionally, the electronegativity of Si (1.09) is less than that of C. Co-doping N and Si, with electronegativities greater and less than that of C, respectively, leads to an optimized electronic structure of PTh.[16,24,25]

The cathodic HER is accompanied by the production of oxygen at the anode. In a hybrid microbial−inorganic catalysis system utilizing aerobic microorganisms, the cathode and anode are housed within a single chamber. Since standard thermodynamic potentials of oxygen reduction are higher than that of HER, oxygen produced by the anode is reduced at the cathode under the HER cathode potential. Oxygen undergoes two pathways: a four-electron pathway to produce water and a two-electron pathway to produce reactive oxygen species (ROS) such as H_2O_2, $O_2^{\bullet-}$, and $^{\bullet}OH$. For microorganisms in electrochemical systems, the generated ROS have damaging effects on their DNA, proteins, lipids, etc., thus inhibiting its metabolism and growth.[6,26] Therefore, eliminating ROS production is another important consideration for biocompatible HER catalysts design. The key step of producing ROS originated from O_2 reduction is the formation of O−O bonds.[27] Heteroatom-doping induces charge redistribution and changes the oxygen adsorption model to weaken O−O bonds.[28] Therefore, doping heteroatoms such as N and Si to design a rational carbon active center can reduce the ROS yield, thereby further enhancing the biocompatibility.

Herein, we innovatively introduced the conductive polymer polythiophene as a substrate of an electrocatalyst. A N- and Si-doped polythiophene nanocomposite (PTh-NSi) was prepared as a nonmetal HER electrocatalyst through ball-milling and hydrothermal treatment. Coupled with PTh-NSi, *Ralstonia eutropha* H16 (*R. eutropha* H16) was employed as a microbial catalyst to construct the hybrid microbial−inorganic catalysis system, converting CO_2 to poly-β-hydroxybutyrate (PHB). PTh-NSi was characterized and HER performance was studied. To evaluate the biocompatibility of PTh-NSi, ROS production during water electrolysis and the interactions between PTh-NSi and *R. eutropha* H16 were systematically studied. The operating parameters and conditions of the hybrid microbial−inorganic catalysis system were optimized to increase PHB production efficiency. Eventually, the coupling mechanism between PTh-NSi and *R. eutropha* H16 was revealed.

2. EXPERIMENTAL SECTION

2.1. Materials. Ferric chloride ($FeCl_3$), thiophene, and urea were purchased from Aladdin Co., Ltd. (Shanghai, China) and used without further purification. Acetone, hydrochloric acid, chloroform, sodium silicate dihydrate ($Na_2SiO_3{\cdot}9H_2O$), and ammonium persulfate ($(NH_4)_2S_2O_8$) were purchased from Macklin Biochemical Co., Ltd. (Shanghai, China) and used without further purification. Unless otherwise specified, all solutions were prepared using purified water. Minimal medium (MM) was composed of 9 g/L $Na_2HPO_4{\cdot}12H_2O$, 3 g/L KH_2PO_4, 0.2 g/L $(NH_4)_2SO_4$, 0.15 g/L $MgSO_4{\cdot}7H_2O$, 0.3 g/L $NaHCO_3$, 50 mg/L ferric citrate, 1.5 mg/L NTA, 0.3 mg/L H_3BO_3, 0.2 mg/L $CoCl_2{\cdot}6H_2O$, 0.1 mg/L $ZnSO_4{\cdot}7H_2O$, 0.03 mg/L $MnCl_2{\cdot}4H_2O$, 0.03 mg/L $Na_2MoO_4{\cdot}2H_2O$, 0.02 mg/L $NiCl_2{\cdot}6H_2O$, and 0.01 mg/L $CuSO_4{\cdot}5H_2O$.

2.2. Synthesis of Catalysts. *2.2.1. Synthesis of SiO_2 Nanodots (SiO_2-NDs).* A 3.7 g portion of $Na_2SiO_3{\cdot}9H_2O$ was dissolved in 100 mL of H_2O, and hydrochloric acid was added to adjust the pH to 6. The suspension was transferred to a Teflon-lined stainless steel autoclave and heated at 160 °C for 14 h. The ground mixture was

https://doi.org/10.1021/cbe.4c00156
Chem Bio Eng. 2025, 2, 229−240

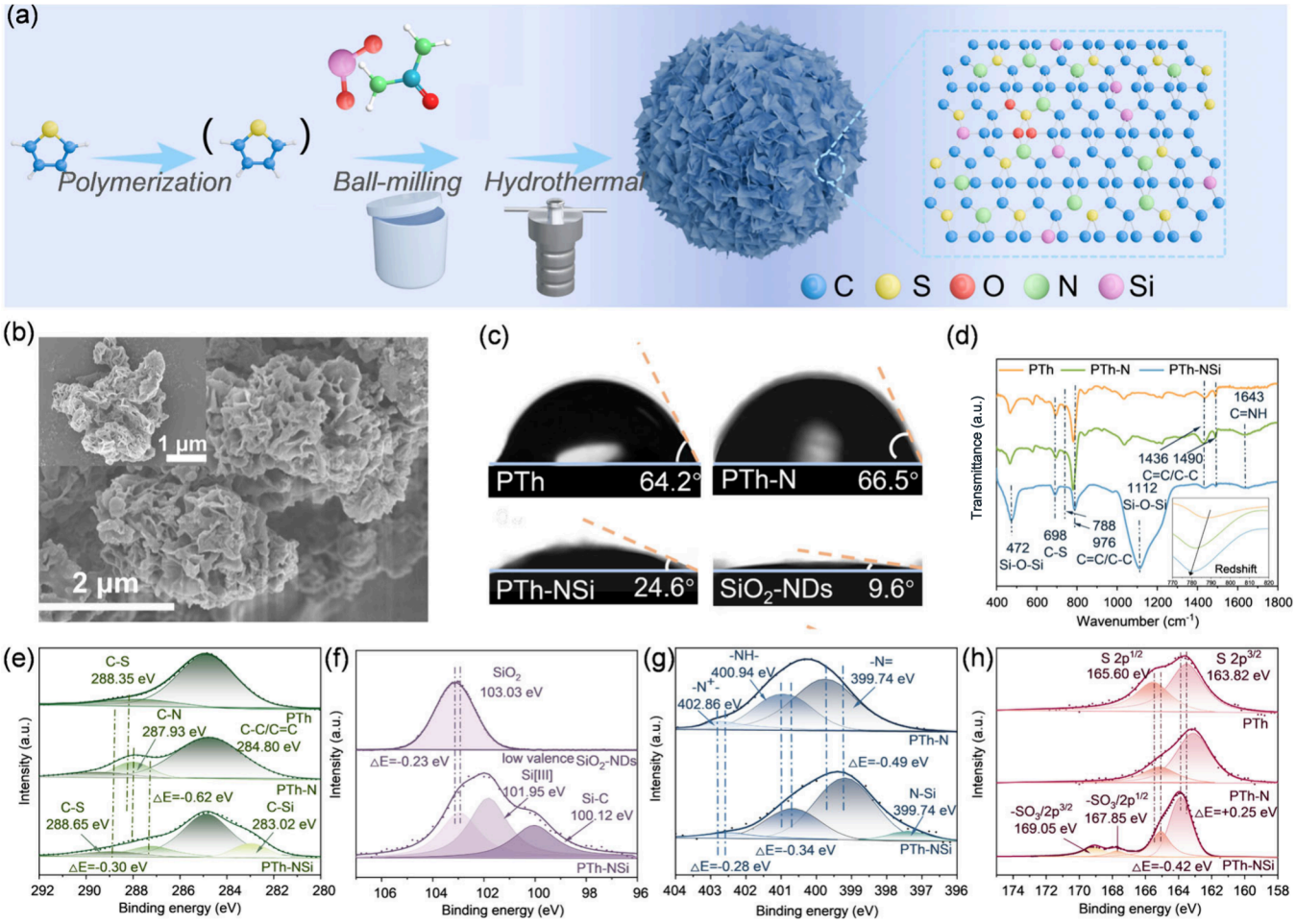

Figure 1. Preparation and characterization of PTh-NSi. (a) The schematic procedure for synthesizing PTh-NSi; (b) SEM image of PTh-NSi; (c) contact angles of PTh-NSi, PTh-N, PTh, and SiO_2-NDs; (d) FT-IR spectra of all samples; (e) high-resolution XPS C 1s spectra of all samples; (f) high-resolution XPS Si 2p spectra of SiO_2-NDs and PTh-NSi; (g) high-resolution XPS N 1s spectra of PTh-N and PTh-NSi; and (h) high-resolution XPS S 2p spectra of all samples.

then annealed under an argon atmosphere at a heating rate of 5 °C min^{-1} for 12 h at 550 °C.

2.2.2. Synthesis of PTh, PTh-N, and PTh-NSi. A 4.86 g portion of $FeCl_3$ was dissolved in 50 mL of chloroform to obtain a dark green solution. Nitrogen was introduced to remove the air in the reaction flask and 0.84 g of thiophene was added, and the reaction was maintained at 0 °C for 12 h. Twenty milliliters of acetone was added to terminate the reaction. The liquid was evaporated and washed repeatedly with 0.1 mol/L HCl, acetone, anhydrous ethanol, and H_2O three times in turn and dried under vacuum at 60 °C for 12 h to obtain PTh. PTh, urea, and SiO_2-NDs in appropriate mass ratios were placed in a ball milling jar and ball milled at 500 rpm for 1 h to obtain the precursor. To 0.5 g of precursor dispersed in H_2O (40 mL) was added 5.4 g of $(NH_4)_2S_2O_8$ to obtain the suspension. The suspension was transferred to a 100 mL Teflon-lined stainless steel autoclave and heated at 140 °C for 24 h. After cooling to room temperature, PTh-NSi was obtained by washing with H_2O three times. A similar method was taken to prepare PTh-N. For information of characterizations, refer to Text S1.

2.3. Electrochemical Measurements. All electrochemical experiments were performed in a typical three-electrode system and tested by an electrochemical workstation CHI 760E (Shanghai, China). Graphite rods were used as counter electrodes, saturated Ag/AgCl was used as reference electrodes, and the electrolyte was 1 M phosphate buffer solution (PBS) (pH = 7.2, Aladdin). The carbon paper was cut to a suitable shape to control the working area in the electrolyte to 2 × 2 cm^2. For more details of electrode preparation, refer to Text S2. For the digital photos of fabricated electrodes (on stainless steel and carbon paper), refer to Figure S3. The linear voltammetry scanning (LSV) parameters were voltage window −0.6 to −1.0 V (vs Ag/AgCl), sweep rate 5 mV/s. The measured potential was converted by E (vs RHE) = E (vs Ag/AgCl) + 0.197 + 0.0592 × pH. The electrochemical active surface area (ECSA) was estimated by determining the double-layer capacitances (C_{DL}). Cyclic voltammetry tests were performed in the non-Faraday region (0.492−0.592 V vs RHE) at scanning speeds of 20−100 mV/s. C_{DL} was obtained by plotting the linear relationship between j_a−j_c (oxidation current−reduction current) at E = 0.542 V (vs RHE) (midpoint of the non-Faraday voltage window) and scanning speed, with C_{DL} being twice the slope. Electrochemical impedance (EIS) was examined over a frequency range of 0.1 MHz to 0.01 mHz. For more details of rate of hydrogen production, refer to Text S2. For measurements of ROS, refer to Text S3.

2.4. Hybrid System Construction. *2.4.1. Preparation of Reactors.* Carbon paper and stainless steel (SS) were cut to 2 × 2 cm^2. Catalyst ink was applied by spraying it on the dried carbon paper. SS was ultrasonically washed with acetone and ethanol in turn for 30 min and dried. A single enclosed chamber reactor was used, with a Pt mesh (1 × 1 cm^2) for the counter electrode and saturated Ag/AgCl for the reference electrode. A 0.22 μm PTFE membrane gas filter was connected to the gas inlet and outlet at the top of the reactor. The two working electrodes and the reference electrode were sterilized by ultraviolet light before use, and all other items were sterilized at 121 °C before use. For more details of hybrid system operation, refer to Text S4.

https://doi.org/10.1021/cbe.4c00156
Chem Bio Eng. 2025, 2, 229−240

2.4.2. Cultivation of R. eutropha H16. *R. eutropha* H16 was precultured in Luria−Bertani medium for 12 h. Subsequently, the bacterial fluid was added to the MM supplemented with D-fructose (10 mg/mL) and precultured again for 12 h. The bacterial fluid was centrifuged three times at 8000 rpm, 10 min to remove fructose residue. The obtained bacterial sediment was dispersed by MM and then inoculated into the reactor. Gentamicin (10 μg/mL) was added to prevent contamination by stray bacteria, and the total volume of MM was controlled to be 125 mL. The initial absorbance at 600 nm was measured by a UV−vis spectrophotometer (Thermo Scientific Evolution 201, USA), which required a range of 0.2−0.4. For the digital images of the reactor, refer to Figures S1 and S2. For more details of determination of metal leaching, extracellular polymers (EPS), confocal laser scanning micrographs (CLSM), and atomic force microscopy (AFM), refer to Text S5.

2.4.3. Quantification of PHB and Biomass. The bacterial sediment was dried at 60 °C, 1 mL of 98 wt % H_2SO_4 was added, the mixture was heated in a water bath at 90 °C for 1 h, and then the solution was shaken well to fully dissolve. The obtained solution was diluted by deionized water in appropriate multiplicity, shaken well, and filtered with a 0.22 μm membrane filter. PHB was determined by high-performance liquid chromatography (HPLC, Agilent HPLC 1260, USA) with the following parameters: chromatographic column Aminex hpx-87H (300 mm × 7 8 mm, Biorad), injection volume 100 μL, column temperature 30 °C, mobile phase 2.5 mM aqueous H_2SO_4 solution, flow rate 0.5 mL/min, UV detector wavelength 210 nm. The concentration of biomass was calculated according to the following equations:[11]

$$c_{\text{biomass}} = 448\ \text{mg L}^{-1} \times \left(\text{OD}_{600} - \frac{c_{\text{PHB}}(\text{mg L}^{-1})}{831\ \text{mg L}^{-1}} \right)$$

$$\text{PHB/DCW} = c_{\text{PHB}}/c_{\text{biomass}}$$

3. RESULTS AND DISCUSSION

3.1. Synthesis and Characterization of Nonmetal HER Electrocatalysts PTh-NSi. The thiophene monomer was polymerized by chemical oxidation to form PTh, which was subsequently combined with urea and SiO_2-NDs by ball-milling and hydrothermal treatments to prepare PTh-NSi (Figure 1a). Single N-doped PTh-N and no-doped PTh were prepared by a similar method as well. After ball-milling and hydrothermal treatments at high temperatures, more defects and/or edges were produced in PTh, which favored the doping of N and Si.[29,30] Meanwhile, the temperatures were not high enough to disrupt the original conjugated structure of PTh. The SEM images (Figure 1b) confirmed that the obtained PTh-NSi had an abundance of irregular distinct fold-like structures. The porous structure with extensive stacking was consistent with nitrogen adsorption/desorption isotherms (Figure S4), and PTh-NSi (151.67 m^2/g) exhibited the highest BET specific surface area compared to PTh (40.13 m^2/g) and PTh-N (92.05 m^2/g). This may be due to the addition of different substances (SiO_2 and urea) leading to different degrees of thermal diffusion during heat treatments. According to the pore structure distributions, PTh-NSi had significantly more mesoporous channels around 5 nm compared to PTh-N and PTh (Figure S5). Mesoporous structure provided larger specific area and more active sites, which was beneficial for the adsorption and separation of small molecules (such as H_2) compared to large porous. Energy dispersive spectrometer (EDS) images (Figure S6) demonstrated that a variety of nonmetal elements (C, N, S, Si) achieved uniform doping. The survey XPS spectrum (Figure S7) was also proof of successful doping and demonstrated that PTh-NSi was not doped with metallic elements, indicating that the high-performance of HER was fully contributed to by nonmetal composition. Contact angle measurements were performed to assess the hydrophilicity of the catalyst (Figure 1c). Before and after Si was doped (PTh-N and PTh-NSi), the contact angle was reduced from 66.5° to 24.6°. The smaller contact angle indicated that Si-doping significantly improved the hydrophilic properties. Successful modification greatly alleviated the blockage of water adsorption and activation in the neutral electrolyte required by microorganisms.

The structure of the obtained PTh-NSi was further characterized to provide detailed insights into its composition and chemical states. As XRD patterns in Figure S8 show, all of the samples showed a wide dispersion peak at ∼20°. This was due to that while $\pi-\pi$ conjugation existed in PTh, the irregular side chains led to an overall amorphous structure.[31,32] After doping with N, the characteristic peaks of urea were present on top of the broad diffraction peaks. Doping with Si made the characteristic peaks of urea weaker and broader, which indicated a poorer crystallinity of PTh-NSi. More insight into the electronic structure in PTh-NSi was gained by high-resolution XPS spectra. Figure 1e displays the high-resolution C 1s spectra. With the introduction of N and Si, distinct peaks at 287.93 and 283.02 eV were newly observed, which can be attributed to C−N and C−Si.[24,33−35] The narrowing of the C−C/C=C bond peaks indicated a modification of the electronic structure. Meanwhile, the C−S and C−N characteristic peaks of PTh-NSi were negatively shifted compared to PTh-N, indicating an increase in electron density around C atoms. Such electron migration formed PTh-NSi a larger $\pi-\pi$ conjugated system in the carbon chain segments than PTh and PTh-N that allowed for more space for delocalized space of electrons.[23,36] The high-resolution Si 2p spectra of PTh-NSi and SiO_2-NDs (Figure 1f) indicated that the Si 2p peaks of PTh-NSi were similarly negatively shifted compared to those of SiO_2-NDs. The newly revealed two peaks of Si−C and low valence state Si [III] indicated that some of the Si was coordinated with C or formed a low valence state Si^{3+} after doping.[23,37,38] Such electron migration increased the electron density around Si atoms. $_{29}$Si magic angle spinning (NMR) MAS spectra (Figure S9) demonstrated the similar phenomenon. The peaks of −112.1, −103.5, and −97.5 ppm revealed in SiO_2-NDs were attributed to the Q_4, Q_3, and Q_2 structures, which were characteristic peaks of SiO_2.[37,39] The dominant Q_4 structure in PTh-NSi was positively shifted by 1.3 ppm, indicating that the electron density around the Si atoms of PTh-NSi was higher than that of SiO_2-NDs. The findings in Si 2p spectra and $_{29}$Si NMR MAS spectra indicated jointly that Si received extra electrons.

N 1s spectra (Figure 1g) showed that N existed in multiple forms (−N^+−, −NH−, and −N=) in PTh-N. A new spectral peak of N−Si revealed after doping with Si, while there were positive shifts in the binding energy of the three N 1s peaks, representing an electron efflux and a decrease in the electron density around N atoms.[40,41] S 2p spectra led to the same finding (Figure 1h), with the positive shifts of S $2p^{1/2}$ and S $2p^{3/2}$ indicating electron efflux from S. The newly revealed peaks of 167.9 and 169.2 eV were attributed to −SO_3H functional group.[30] The appearance of a new group provided important evidence for the realization of electronic modulation.

FT-IR similarly confirmed the above point about electron modulation (Figure 1d). The band around 698 cm^{-1} in all

https://doi.org/10.1021/cbe.4c00156
Chem Bio Eng. 2025, 2, 229−240

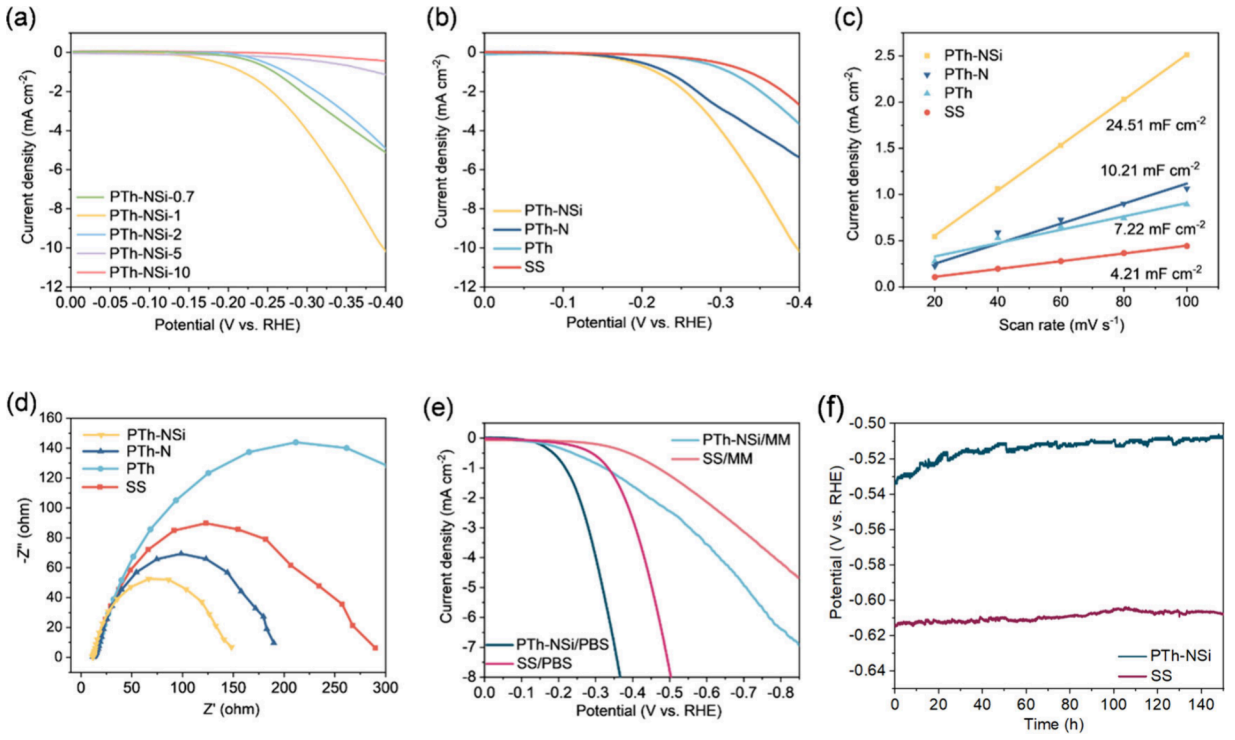

Figure 2. Electrochemical characterizations. (a) LSV curves of PTh-NSi with different mass ratios of SiO_2/PTh; (b) LSV curves of all samples in 1 M PBS with a scan rate of 5 mV/s; (c) the plot of the capacitive current at 0.54 V of all samples against the scan rate in 1 M PBS; (d) Nyquist plot of electrochemical impedance spectra of all samples; (e) LSV curves of PTh-NSi and SS in N_2-saturated MM with a scan rate of 5 mV/s; and (f) chronoamperometric measurements of the long-term stability of PTh-NSi and SS at current density of 5 mA/cm^2.

samples was attributed to the C−S band, which was a characteristic band of the thiophene ring.[42,43] The broad bands at 1112 and 472 cm^{-1} in PTh-NSi represented a bond of Si−O−Si. The band of Si−C at 1200 cm^{-1} and the $-SO_3$ group at 1147 cm^{-1} were covered off because the intensity of the Si−O−Si band was too high. The widespread multiple bands at 788, 976, 1436, and 1490 cm^{-1} were attributed to C=C/C−C.[31] Redshifts appeared due to multielement doping with N and Si, again representing migration of electrons toward the carbon chain and an increasing delocalized space of electrons, consistent with XPS C 1s results. The characteristic C−H band of the aromatic ring at 1173 cm^{-1} in the Raman spectra (Figure S10) proved that the aromatic structure of PTh was still retained after modification, which was consistent with the finding in FT-IR spectra.[41] Taken together, the results above showed that there were strong electronic interactions between the doped heteroatom and PTh in PTh-NSi.

3.2. Electrochemical Measurement of PTh-NSi as HER Electrocatalysts. In hybrid microbial−inorganic catalysis systems, *R. eutropha* H16 uses electrons carried by hydrogen for the conversion of CO_2 to PHB. Before applying into a hybrid catalysis system, the HER performance of samples was first determined by LSV in 1 M PBS solution (pH = 7.2). In previous work of hybrid inorganic−microbial catalysts, SS was commonly used as the cathode.[7,44−48] SS was used as a comparison. The ratio of N-doping and PTh was chosen with reference to the previous reports, and the same chemical amount ratio (0.2) was chosen.[24] LSV curves of PTh-NSi with different SiO_2/PTh mass ratios were shown in Figure 2a. When the SiO_2/PTh mass ratio was 1, PTh-NSi achieved the highest catalytic activity. The SiO_2-NDs/PTh mass ratio was therefore kept at 1 in all of the following experiments. As the LSV curves showed in Figure 2b, compared with PTh-N, PTh, and SS, PTh-NSi delivered the lowest overpotential of −0.395 V (vs RHE) at a current density of 10 mA/cm^2. The Tafel slope of 175 mV/dec for PTh-NSi was much lower than that of PTh (327 mV/dec), PTh-N (195 mV/dec), and SS (199 mV/dec), indicating that PTh-NSi possessed the best kinetics of HER in PBS solution (Figure S11). The hydrogen production rates of all the samples determined by gas chromatography at −1.0 V (vs RHE) also confirmed that PTh-NSi delivered the best HER performance (Figure S12). Figure 2c and Figure S13 showed that the C_{DL} of PTh-NSi was 24.51 mF/cm^2, which was much higher than that of 10.21 mF/cm^2 for PTh-N, 7.22 mF/cm^2 for PTh, and 4.21 mF/cm^2 for SS. C_{DL} was positively correlated with ECSA. The higher ECSA of PTh-NSi was consistent with the nitrogen adsorption/desorption isotherms results to some extent, indicating that the process of doping with heteroatoms (N, Si) by heat-treatment obtained abundant defect structures and effectively enhanced the HER performance. Furthermore, EIS as shown in Figure 2d indicated that PTh-NSi had the lowest charge transfer resistance compared to other samples. This meant, although SiO_2-NDs was an insulating material, doping with N and Si moderated the charge density. The larger electron cloud formed around the carbon chain contributes to the fast electron transfer, consistent with high-resolution C 1s spectra and FT-IR.

LSV curves were performed in MM to further illustrate the HER performance of PTh-NSi in MM (Figure 2e). Due to the fact that the ionic strength of MM (∼72 mM/kg) was much lower than that of 1 M PBS (∼2000 mM/kg), the overpotential of both PTh-NSi and SS increased. The overpotential of PTh-NSi at 5 mA/cm^2 was 654 mV, which was still lower than SS (824 mV), exhibiting better catalytic

https://doi.org/10.1021/cbe.4c00156
Chem Bio Eng. 2025, 2, 229−240

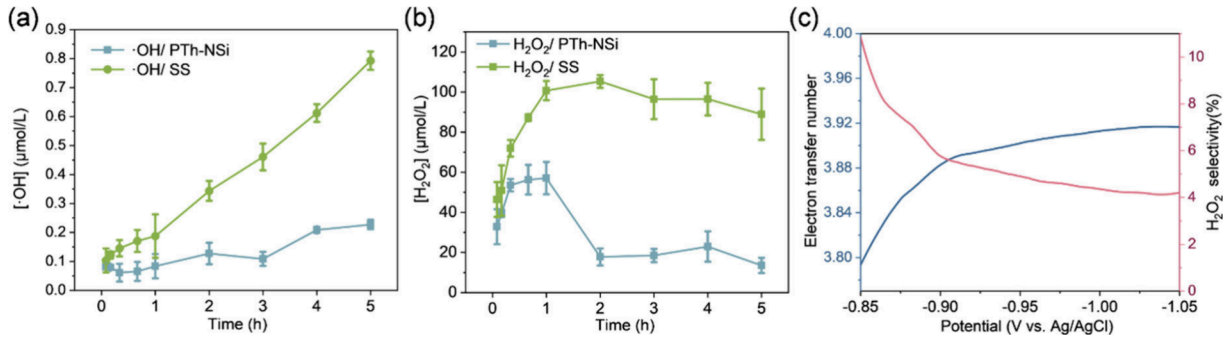

Figure 3. ROS assessment. Assay of (a) •OH and (b) H_2O_2 of PTh-NSi and SS and (c) H_2O_2 selectivity and electron transfer number of PTh-NSi.

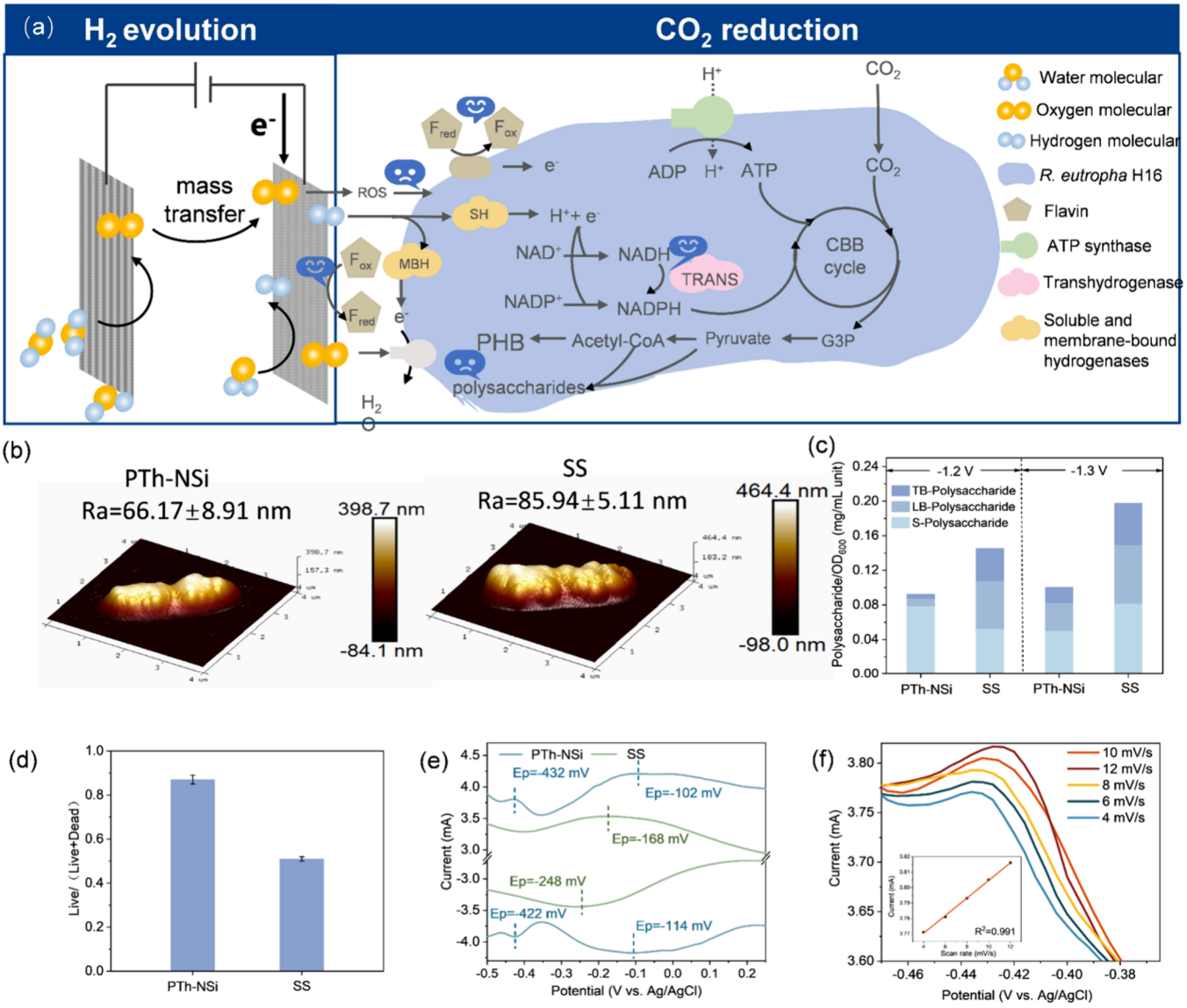

Figure 4. (a) Interactions between *R. eutropha* H16 and PTh-NSi and SS cathode; (b) AFM images of *R. eutropha* H16; (c) polysaccharide/OD_{600} at −1.2 and −1.3 V; (d) survival percentage of *R. eutropha* H16 with PTh-NSi cathode and SS cathode; (e) DPV curves; and (f) DPV curves with different scan rates with the PTh-NSi cathode (inset: relationship between peak heights and scan rates).

activity in MM. The Tafel slope of PTh-NSi in MM was 548 mV/dec, which was lower compared to 755 mV/dec of SS (Figure S14). In a hybrid catalysis system, microorganisms attached to the electrodes were unable to tolerate high current densities (>10 mA/cm^2). Therefore, chronoamperometric measurements of the long-term stability of PTh-NSi and SS were performed at a current density suitable for microbial growth (5 mA/cm^2). It showed that PTh-NSi could be operated stably for more than 150 h at the given current density, while the operating voltage is about 100 mV lower

https://doi.org/10.1021/cbe.4c00156
Chem Bio Eng. 2025, 2, 229−240

than that of SS (Figure 2f). Table S1 listed the HER performance comparison of PTh-NSi with some representative nonmetal electrocatalysts in previous studies, which showed that PTh-NSi lead the competition in both HER performance and stability. Long-cycle operation stability of PTh-NSi matched with the following microorganism growth cycle (7−10 days).

3.3. ROS Evaluation with PTh-NSi as HER Electrocatalysts. Since ROS (including H_2O_2, $^{\bullet}OH$, and $O_2^{\bullet-}$) caused oxidative damage to microorganisms, its production was an important factor to evaluate the biocompatibility of HER electrocatalysts. Standard thermodynamic potentials were 0.083 V for H_2O_2, 0.113 V for $^{\bullet}OH$, −0.527 V for $O_2^{\bullet-}$, and −0.607 V for hydrogen (pH = 7, vs statured Ag/AgCl).[6,7] Such a difference of thermodynamic potential made ROS production dominant at or below the potential of generating hydrogen in a neutral electrolyte (i.e., MM). Therefore, quantification of $^{\bullet}OH$ and H_2O_2 was performed at low cathodic potential (−1.1 V) that was more likely to produce ROS. $^{\bullet}OH$ with PTh-NSi and the SS cathode showed an overall trend of increasing concentration over time (Figure 3a). The concentration of $^{\bullet}OH$ produced by PTh-NSi (0.22 μmol/L at 5 h) was only 28% of that produced by SS (0.79 μmol/L at 5 h, Figure 3a). As for H_2O_2 production shown in Figure 3b, the H_2O_2 produced by the PTh-NSi cathode reached a peak (57 μmol/L) at 1 h and then gradually dropped to 20 μmol/L at 5 h. Meanwhile, the concentration of H_2O_2 produced by the SS cathode produced a higher H_2O_2 concentration than PTh-NSi cathode, reaching a maximum of 105 μmol/L at 2 h and remained at 90 μmol/L thereafter. This was probably due to the presence of metal ions in MM catalyzing the Fenton/Fenton-like reaction of oxidizing H_2O_2 to produce $^{\bullet}OH$. Metal ions (Fe^{3+}, Ni^{2+}, Cr^{3+}, etc.) leached by SS catalyze H_2O_2 more, resulting in $^{\bullet}OH$ in a greater content (Figure S15). All metal leaching with PTh-NSi showed an overall decreasing trend, which was due to the nonmetal composition of PTh-NSi, and microbes utilize metal ions in the solution. For example, microbes utilize Fe and Ni to synthesize [NiFe] hydrogenase, which is the crucial redox center for electron transfer processes. Meanwhile, there is no highly toxic Cr in the electrolyte with the PTh-NSi cathode. To clarify effects of H_2O_2 on *R. eutropha* H16, survival rates of *R. eutropha* H16 with different concentrations of H_2O_2 were evaluated by the cell counting method. As shown in Figure S16, 100 μmol/L H_2O_2 killed 24% of *R. eutropha* H16 and 20 μmol/L H_2O_2 killed 5.2% of *R. eutropha* H16. Due to the instantaneous production of $^{\bullet}OH$ and its extremely short half-life (10^{-9} s), it was difficult to quantify the effects of different concentrations of $^{\bullet}OH$ on *R. eutropha* H16. It had been previously reported that the inactivation process of microorganisms was promoted when the production of $^{\bullet}OH$ was promoted.[49,50] It followed that PTh-NSi was biocompatible due to the low ROS yield.

The lower ROS yield was attributed to the electron pathway of oxygen reduction (Figure 3c). It showed that oxygen mainly underwent a four-electron pathway reduction to H_2O (electron transfer number $n \approx 3.9$) rather than two-electron pathway to H_2O_2 with PTh-NSi cathode, and the selectivity of O_2 reduction to H_2O_2 was less than 8% (Figure S17a). This more desirable electron transfer pathway was attributed to the doping of N and Si. For the undoped thiophene ring, the spin scheme on the C atom facilitates oxygen adsorption and reformation of the O−O bond for reduction to H_2O_2. It turned out the heteroatom-doping significantly enhanced the electron transfer number and reduced the H_2O_2 selectivity on the basis of PTh (Figures S17b and S17c). Doping with heteroatoms altered the intrinsic electronic properties of PTh and enhanced electron transfer between C and heteroatoms.[17,27] It resulted in a greater tendency to break the O−O bonds and eventually produce H_2O (four-electron pathway). Altogether, the heteroatom-doping strategy not only improved HER performance but also enhanced biocompatibility by decreasing ROS yield.

3.4. Interactions between PTh-NSi Cathode and *R. eutropha* H16. EPS including proteins, polysaccharides, nucleic acids, lipids, etc., played important roles in the interactions between the electrode and microorganisms. Meanwhile, the secretion of EPS was significantly affected by the extracellular environment. The relatively smooth exterior of *R. eutropha* H16 was roughened by loosely bound EPS (LB-EPS) and toughly bound EPS (TB-EPS), which was visualized by AFM. Roughness of *R. eutropha* H16 with the PTh-NSi cathode was ∼23% lower than that with the SS cathode (66.17 ± 8.91 nm vs 85.94 ± 5.11 nm, n = 24), indicating differences in EPS secretion (Figure 4a). Among all components of EPS, polysaccharide was usually considered to provide bacteria protection from a wide range of stresses as a protective barrier for microorganisms. Especially, polysaccharides were generally considered as significant antioxidants by reducing ROS and metal ions.[51] Therefore, total polysaccharides/OD_{600} was used to reveal the interaction between the cathodes and microorganisms and evaluate the biocompatibility of the PTh-NSi cathode. At the end of two independent operation cycles (applied voltage of −1.2 and −1.3 V), total polysaccharides/OD_{600} in the systems using PTh-NSi cathodes were around 64% (−1.2 V) and 52% (−1.3 V) those with the SS cathode, respectively (Figure 4b). This was because the SS cathode induced higher adverse environmental stress during water electrolysis, stimulating *R. eutropha* H16 to produce more extracellular polysaccharides for a protective strategy.[52,53] Meanwhle, images of flow cytometry showed that survival rates of *R. eutropha* H16 with the PTh-NSi cathode were 70% higher than that with the SS cathode (Figures 4d and S18), which was the highest among the relevant studies. Thereby, the lower polysaccharides/OD_{600} indicated that PTh-NSi cathodes were more biocompatible compared to the SS cathode.

Extracellular electron transfer, including direct and indirect pathways, was another important consideration in the interaction between the cathode and *R. eutropha* H16. Formation of biofilms on the cathode could enable a direct electron transfer pathway. Thus, CLSM with live/dead bacterial staining were employed to image the biofilm formation on both cathodes (Figure S19). CLSM results showed that there was more uniform biofilm attachment on the PTh-NSi cathodes, while the overall biomass was lower, and most of the bacteria were dead. This was due to the strong hydrogen production reaction on the electrode surface and the high levels of ROS in the microenvironment of the electrode surface. Given that there was no active biofilm formation on either the PTh-NSi or SS electrodes, direct electron transfer could be neglected. Beside direct electron transfer and H_2 mediated electron transfer, indirect electron transfer depended on molecules with redox activity such as flavin, methylviologen, quinone analogues, and neutral red as electron shuttles which might also exist between the cathode and microorganisms. Therefore, differential pulse voltammetry (DPV) was performed to determine the existence of electron shuttles for

https://doi.org/10.1021/cbe.4c00156
Chem Bio Eng. 2025, 2, 229−240

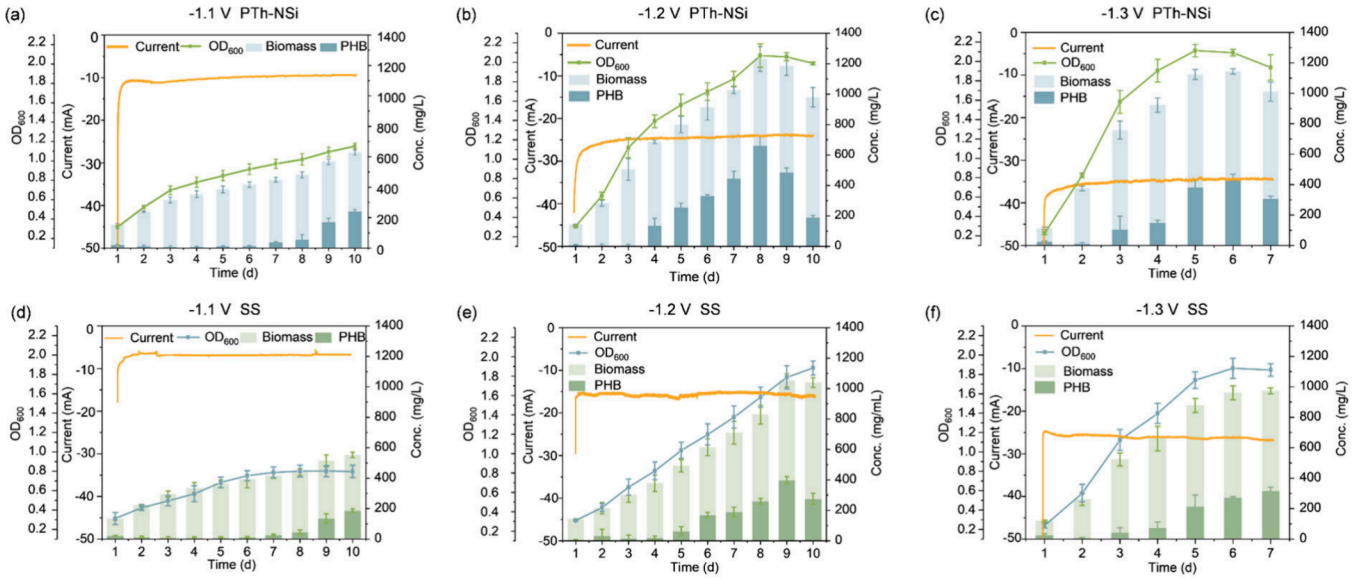

Figure 5. Current, *R. eutropha* H16 growth, and electrochemical synthesis in a hybrid inorganic−microbial catalysis system with a PTh-NSi cathode at (a) −1.1, (b) −1.2, and (c) −1.3 V and an SS cathode at (d) −1.1, (e) −1.2, and (f) −1.3 V.

indirect electron transfer in our system. DPV curves obtained with a PTh-NSi cathode showed two pairs of peaks (Figure 4e). One pair was E_p = −432 mV (anodic potential, versus saturated Ag/AgCl, the same as below) and E_p = −422 mV (cathodic potential) (Figure 4d). According to a previous publication, this pair of peaks was likely attributed to flavin.[54] Notably, the presence of flavin was not observed in the DPV curves with the SS cathode. To further confirm the existence of flavin, the electrolyte was qualitatively detected by LC-MS with a secondary MS analysis. The MS result showed that the 377.2 peak yielded an ion with a m/z ratio of 243, consistent with riboflavin standards (Figure S20). In addition, the heights flavin peak increased as a linear function of scan rate (R = 0.990), which was evidence for the adsorption of flavin to PTh-NSi electrode (Figure 4e).[55] This was due to the multiple N sites on the PTh-NSi cathode, which could adsorb flavin on the surface.[56] Meanwhile, Si-doping improved the hydrophilicity of the PTh-NSi cathode and also contributed to the adsorption of the hydrophilic flavin.[57] The adsorption accelerated the reduction of riboflavin and thus increased the turnover frequency of riboflavin as an electron shuttle, which boosted indirect electron transfer between the cathode and *R. eutropha* H16. To further confirm the effect of indirect electron transfer on the bacterial metabolism, *R. eutropha* H16 were transferred to a system with fresh MM and a new PTh-NSi cathode, and the ratio of NADPH and $NADP^+$ (NADPH/$NADP^+$) was compared to that of the untransferred *R. eutropha* H16 (Figure S21). The NADPH/$NADP^+$ of untransferred *R. eutropha* H16 was 1.44 times higher than that of the transferred one (72 h), which proved that the presence of indirect electron transfer mediated by flavin could promote the metabolism of *R. eutropha* H16.

3.5. Growth and PHB Production by *R. eutropha* H16 with PTh-NSi as the Electrocatalyst. PTh-NSi was applied to a hybrid microbial−inorganic catalysis system as the electrocatalyst, with SS used for comparison. At various applied voltages (−1.1, −1.2, and −1.3 V), the PTh-NSi cathode consistently showed higher current (11, 25, and 35 mA) compared to SS (7, 16, and 27 mA) (Figure 5). More hydrogen was provided to *R. eutropha* H16 supporting its metabolism and growth, which resulted in higher OD_{600} and PHB production. In particular, the PHB yield of the PTh-NSi cathode (662.99 ± 27.46) was enhanced by 66% compared to SS (397.82 ± 17.82 mg/L). For PTh-NSi, the maximum OD_{600} was 1.19, while the final yield of PHB was 241.9 ± 10.1 mg/L at −1.1 V. As the voltage increased to −1.2 V, the maximum OD_{600} was 2.06 with the maximum PHB yield of 662.99 ± 27.46 mg/L. At −1.3 V, OD_{600} reached the maximum value of 2.1, while maximum PHB yield decreased to 446.97 ± 10.64 mg/L. The increase in OD_{600} and PHB yield from −1.1 to −1.2 V was attributed to the higher hydrogen production by PTh-NSi, as mentioned earlier. However, when voltage varied from −1.2 to −1.3 V, more hydrogen led to faster growth of *R. eutropha* H16. Nonetheless, the PHB yield decreased, which might be due to the negative effect of excessive voltage on the microorganism (~9 mA/cm^2). When microorganisms were subjected to external electric field, a microelectric field was formed on both sides of the membrane. Increasing the strength of the applied electric field increased the membrane permeability, resulting in the death or inactivation of microorganisms. From the perspective of the anodic reaction, hypochlorite or reactive nitrogen species might produce higher voltage, inhibiting the activity of *R. eutropha* H16.[7,58] Several reports demonstrated that increasing the applied voltage in microbial electrosynthesis systems decreased the yield of target products.[59,60] The percentage of alive cells of *R. eutropha* H16 in a hybrid catalysis system at −1.2 and −1.3 V was determined by flow cytometry (Figure S22). The survival rate was 87% at −1.2 V, which was 1.52 times that at −1.3 V (58%). In brief, the PTh-NSi electrocatalyst exhibited outstanding HER performance and biocompatibility, achieving a PHB yield as high as 662.99 ± 27.46 mg/L at −1.2 V, outcompeting most yields previously achieved in hybrid catalysis systems (Table S2). PHB yield was 24% higher than the highest previous yields of similar systems and significantly reduced operation time. Since our electrocatalysts were heat treated at rather low temperatures in order not to destroy the polythiophene structure (compared to calcination, which is most commonly used for catalyst preparation), lower energy consumption opened up the

https://doi.org/10.1021/cbe.4c00156
Chem Bio Eng. 2025, 2, 229−240

possibility of realizing industrial processes. In addition, ball-milling and hydrothermal reactions are controllable during scale-up processes. This also adds reliability for subsequent integration.

The effects of microorganisms and the solution environment on HER electrocatalysts need to be studied to evaluate the stability of PTh-NSi in a microorganism medium. After 10 days of operation, the LSV curves shown in Figure 6a indicated that

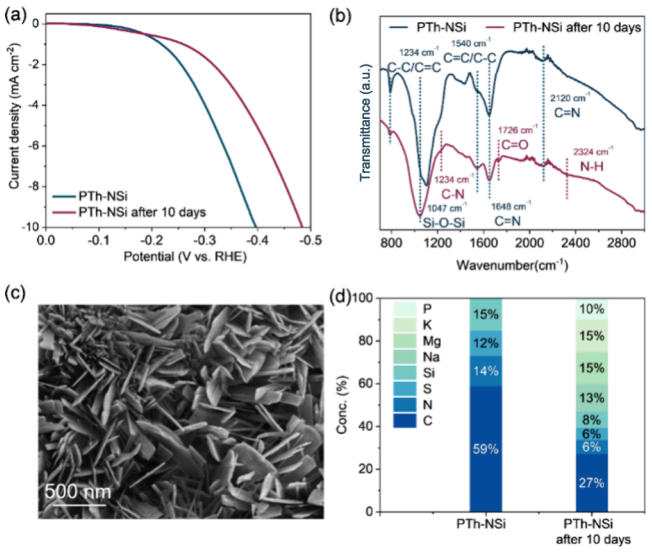

Figure 6. Comparison of the PTh-NSi cathode before and after operation. (a) LSV curves in 1 M PBS; (b) FT-IR; (c) SEM images of the PTh-NSi cathode after operation; and (d) element contents obtained by EDS after operation.

the HER performance of PTh-NSi decayed by approximately 24%. FT-IR was utilized to identify the changes of the functional groups on the electrode surface. The results in Figure 6b showed that new bonds of C=O, C−N, and N−H appeared on the electrodes after the operation, which were originated from the carboxyl and amino functional groups of attached EPS and biomass. Deposition of EPS secreted by *R. eutropha* H16 on the electrodes resulted in performance decay. Furthermore, the SEM image of the used electrode showed a multilayered thick sheet-like crystalline structure (Figure 6c) and Na, K, P, and Mg elements from the electrolyte were identified on the electrodes (Figure 6d and Figure S23), which resulted in the deactivation of the catalytic sites. A possible explanation was negative charge on the electrode surface causing electrostatic adsorption of cations leading to the decrease of HER performance.

4. CONCLUSION

This study demonstrates the successful synthesis and application of a PTh-based nonmetal electrocatalyst, PTh-NSi, for efficient HER and biocompatible conversion of CO_2 to PHB in a hybrid microbial−inorganic catalysis system. The unique electronic modulation strategy used in the synthesis of PTh-NSi, which incorporates N- and Si-doping, significantly enhances the catalytic performance, stability, and biocompatibility of the electrocatalyst. The PTh-NSi electrocatalyst achieved a current density of 10 mA/cm^2 at a low overpotential of −0.395 V in neutral PBS, showing excellent HER activity compared to reported nonmetal HER catalysts in neutral environments. Silicon-doping was particularly effective in promoting hydrophilicity, which is crucial for maintaining efficient catalytic activity in aqueous environments required for microbial growth. The robust structure of PTh enabled stable operation over 150 h, aligning with the growth cycle of *R. eutropha* H16 and facilitating long-term CO_2 conversion. The biocompatibility of PTh-NSi was confirmed through minimal ROS production and the absence of heavy metal ion leaching, which supported the fast growth of *R. eutropha* H16 and enhanced PHB production. The hybrid system achieved a PHB yield of up to 662.99 ± 27.46 mg/L, which is 1.66 times higher than the yield obtained with SS cathodes. The interaction between PTh-NSi and *R. eutropha* H16 led to the secretion of more redox-active proteins and fewer insulating polysaccharides, further revealing the synergistic interactions. Additionally, flavin production by *R. eutropha* H16 coupled with PTh-NSi was confirmed, which facilitated the NADPH/NADP$^+$ balance, enhancing the overall efficiency of the CO_2 conversion. The strategy of introducing a conducting polymer as the substrate and modulating the electron density will provide new ideas for the design of nonmetal catalysts, especially those suitable for hybrid inorganic−microbial catalysis systems. This work paves the way for the development of sustainable and efficient technologies for CO_2 conversion, highlighting the potential of using nonmetal electrocatalysts in microbial−inorganic hybrid systems for environmental and industrial applications.

■ ASSOCIATED CONTENT

Data Availability Statement

All of the important data needed to evaluate the conclusions are present in the article and/or the Supporting Information. Data information for Figures 1, 2a, 2b, 2d−2f, 3c, 4d, 4e, and 6 are available from the corresponding author upon reasonable request. The numerical data from Figures 2c, 4b, and 5 are tabulated in the Supporting Information. Error bars in Figures 3 and 5 show the spread of data observed in triplicate measurements, where samples of independent reactors were tested for each measurement. Experimental data shown without error bars are from individual experimental measurements.

Supporting Information

The Supporting Information is available free of charge at https://pubs.acs.org/doi/10.1021/cbe.4c00156.

Additional experimental details, catalyst characterization, biological experimental characterization and numeral data of figures (PDF)

■ AUTHOR INFORMATION

Corresponding Authors

Zhongjian Li − *College of Chemical and Biological Engineering, Key Laboratory of Biomass Chemical Engineering of Ministry of Education, Zhejiang University, Hangzhou 310027, China;* orcid.org/0000-0002-3685-381X; Email: zdlizj@zju.edu.cn

Min Yao − *School of Civil & Environmental Engineering and Geography Science, Ningbo University, Ningbo 315211, China*; Email: yaomin@nbu.edu.cn

Authors

Xianghai Bian − *College of Chemical and Biological Engineering, Key Laboratory of Biomass Chemical Engineering of Ministry of Education, Zhejiang University, Hangzhou 310027, China*

https://doi.org/10.1021/cbe.4c00156
Chem Bio Eng. 2025, 2, 229−240

Yang Ye − *College of Chemical and Biological Engineering, Key Laboratory of Biomass Chemical Engineering of Ministry of Education, Zhejiang University, Hangzhou 310027, China*
Sulin Ni − *College of Chemical and Biological Engineering, Key Laboratory of Biomass Chemical Engineering of Ministry of Education, Zhejiang University, Hangzhou 310027, China*
Bin Yang − *College of Chemical and Biological Engineering, Key Laboratory of Biomass Chemical Engineering of Ministry of Education, Zhejiang University, Hangzhou 310027, China;* orcid.org/0000-0002-5136-9743
Yang Hou − *College of Chemical and Biological Engineering, Key Laboratory of Biomass Chemical Engineering of Ministry of Education, Zhejiang University, Hangzhou 310027, China;* orcid.org/0000-0001-9795-8503
Lecheng Lei − *College of Chemical and Biological Engineering, Key Laboratory of Biomass Chemical Engineering of Ministry of Education, Zhejiang University, Hangzhou 310027, China*

Complete contact information is available at: https://pubs.acs.org/10.1021/cbe.4c00156

Author Contributions

B.X.: writing−original draft, investigation, formal analysis, and data curation. Y.Y.: data curation and methodology. S.N.: software and visualization. Y.B.: investigation. H.Y.: investigation. L.L.: investigation. Y.M.: writing−review and editing and supervision. L.Z.: writing−review and editing, supervision, funding acquisition, and conceptualization.

Notes

The authors declare no competing financial interest.

■ ACKNOWLEDGMENTS

This work was supported by the Key Research and Development Program of Zhejiang Province (Grant 2024C03111) and the National Natural Science Foundation of China (Grants 22075245 and 22122812).

■ REFERENCES

(1) De Luna, P.; Hahn, C.; Higgins, D.; Jaffer, S. A.; Jaramillo, T. F.; Sargent, E. H. What would it Take for Renewably Powered Electrosynthesis to Displace Petrochemical Processes? *Science* **2019**, *364* (6438), No. eaav3506.
(2) Schmid, A.; Dordick, J. S.; Hauer, B.; Kiener, A.; Wubbolts, M.; Witholt, B. Industrial Biocatalysis Today and Tomorrow. *Nature* **2001**, *409* (6817), 258−268.
(3) Zheng, T.; Zhang, M.; Wu, L.; Guo, S.; Liu, X.; Zhao, J.; Xue, W.; Li, J.; Liu, C.; Li, X.; Jiang, Q.; Bao, J.; Zeng, J.; Yu, T.; Xia, C. Upcycling CO_2 into Energy-Rich Long-Chain Compounds via Electrochemical and Metabolic Engineering. *Nat. Catal.* **2022**, *5* (5), 388−396.
(4) Chen, X.; Cao, Y.; Li, F.; Tian, Y.; Song, H. Enzyme-Assisted Microbial Electrosynthesis of Poly(3-hydroxybutyrate) via CO_2 Bioreduction by Engineered *Ralstonia eutropha*. *ACS Catal.* **2018**, *8* (5), 4429−4437.
(5) Xu, M.; Tremblay, P.-L.; Jiang, L.; Zhang, T. Stimulating Bioplastic Production with Light Energy by Coupling *Ralstonia eutropha* with the Photocatalyst Graphitic Carbon Nitride. *Green Chem.* **2019**, *21* (9), 2392−2400.
(6) Xiu, S.; Lu, J.; Guo, Y.; Li, Y.; Liu, F.; Yao, J.; Wu, H.; Yang, B.; Hou, Y.; Lei, L.; Li, Z. Confinement Strategy to Boost the Compatibility of Hybrid Microbial-Inorganic Catalysis for Highly Efficient CO_2 Reduction. *Chem. Eng. J.* **2023**, *474*, No. 145407.
(7) Torella, J. P.; Gagliardi, C. J.; Chen, J. S.; Bediako, D. K.; Colón, B.; Way, J. C.; Silver, P. A.; Nocera, D. G. Efficient Solar-to-Fuels Production from a Hybrid Microbial−Water-Splitting Catalyst System. *Proc. Natl. Acad. Sci. U. S. A.* **2015**, *112* (8), 2337−2342.
(8) Wu, H.; Pan, H.; Li, Z.; Liu, T.; Liu, F.; Xiu, S.; Wang, J.; Wang, H.; Hou, Y.; Yang, B.; Lei, L.; Lian, J. Efficient Production of Lycopene from CO_2 via Microbial Electrosynthesis. *Chem. Eng. J.* **2022**, *430*, No. 132943.
(9) Wang, Y.; Zhang, C.; Li, X.; Gao, T.; Wang, X.-B. Metal-free Carbon-Based Nanomaterials for Electrochemical Nitrogen and Carbon Dioxide Reductions. *Mater. Res. Bull.* **2021**, *140*, No. 111294.
(10) Liu, X.; Dai, L. Carbon-based Metal-Free Catalysts. *Nat. Rev. Mater.* **2016**, *1* (11), No. 16064.
(11) Liu, C.; Colon, B. C.; Ziesack, M.; Silver, P. A.; Nocera, D. G. Water Splitting-Biosynthetic System with CO_2 Reduction Efficiencies Exceeding Photosynthesis. *Science* **2016**, *352* (6290), 1210−1213.
(12) Wang, R.; Li, H.; Sun, J.; Zhang, L.; Jiao, J.; Wang, Q.; Liu, S. Nanomaterials Facilitating Microbial Extracellular Electron Transfer at Interfaces. *Adv. Mater.* **2021**, *33* (6), No. 2004051.
(13) Bendrea, A.-D.; Cianga, L.; Cianga, I. Review paper: Progress in the Field of Conducting Polymers for Tissue Engineering Applications. *J. Biomater. Appl.* **2011**, *26* (1), 3−84.
(14) Wong, J. Y.; Langer, R.; Ingber, D. E. Electrically Conducting Polymers can Noninvasively Control the Shape and Growth of Mammalian Cells. *Proc. Natl. Acad. Sci. U. S. A.* **1994**, *91* (8), 3201−3204.
(15) Xiang, H.; Deng, N.; Zhao, H.; Wang, X.; Wei, L.; Wang, M.; Cheng, B.; Kang, W. A Review on Electronically Conducting Polymers for Lithium-sulfur Battery and Lithium-Selenium Battery: Progress and Prospects. *J. Energy Chem.* **2021**, *58*, 523−556.
(16) Zhou, Y.; Leng, Y.; Zhou, W.; Huang, J.; Zhao, M.; Zhan, J.; Feng, C.; Tang, Z.; Chen, S.; Liu, H. Sulfur and Nitrogen Self-doped Carbon Nanosheets Derived from Peanut Root Nodules as High-Efficiency Non-Metal Electrocatalyst for Hydrogen Evolution Reaction. *Nano Energy* **2015**, *16*, 357−366.
(17) Hu, C.; Gao, Y.; Zhao, L.; Dai, L. Carbon-based Metal-free Electrocatalysts: Recent Progress and Forward Looking. *Chem. Catal.* **2022**, *2* (9), 2150−2156.
(18) Wang, G.; Xu, X.; Kou, X.; Liu, X.; Dong, X.; Ma, H.; Wang, D. N-Doping of Graphene Aerogel as a Multifunctional Air Cathode for Microbial Fuel Cells. *ACS Appl. Mater. Interfaces* **2021**, *13* (43), 51312−51320.
(19) Yao, J.; Li, Y.; Xiu, S.; Zheng, S.; Huang, Y.; Zhou, Z.; Hou, Y.; Yang, B.; Lei, L.; Li, Z. Efficient CO_2 Conversion by Biocompatible N-Doped Carbon Nanosheets Coupled with *Ralstonia eutropha*: Synergistic Interactions Between Microbial and Inorganic Catalysts. *Green Chem.* **2023**, *25* (12), 4760−4768.
(20) Ye, J.; Hu, A.; Ren, G.; Chen, M.; Tang, J.; Zhang, P.; Zhou, S.; He, Z. Enhancing Sludge Methanogenesis with Improved Redox Activity of Extracellular Polymeric Substances by Hematite in Red Mud. *Water Res.* **2018**, *134*, 54−62.
(21) Ma, Y.; Fu, Y.; Jiang, W.; Wu, Y.; Liu, C.; Che, G.; Fang, Q. Excellent Electrocatalytic Performance of Metal-free Thiophene−Sulfur Covalent Organic Frameworks for Hydrogen Evolution in Alkaline Medium. *J. Mater. Chem. A* **2022**, *10* (18), 10092−10097.
(22) Zheng, X.; Shi, X.; Ning, H.; Yang, R.; Lu, B.; Luo, Q.; Mao, S.; Xi, L.; Wang, Y. Tailoring a Local Acid-Like Microenvironment for Efficient Neutral Hydrogen Evolution. *Nat. Commun.* **2023**, *14* (1), 4209.
(23) Feng, J.-X.; Xu, H.; Ye, S.-H.; Ouyang, G.; Tong, Y.-X.; Li, G.-R. Silica-Polypyrrole Hybrids as High-Performance Metal-Free Electrocatalysts for the Hydrogen Evolution Reaction in Neutral Media. *Angew. Chem., Int. Ed.* **2017**, *56* (28), 8120−8124.
(24) Domínguez, C.; Pérez-Alonso, F. J.; Abdel Salam, M.; Al-Thabaiti, S. A.; Obaid, A. Y.; Alshehri, A. A.; Gómez de la Fuente, J. L.; Fierro, J. L. G.; Rojas, S. On the Relationship Between N content, Textural Properties and Catalytic Performance for the Oxygen Reduction Reaction of N/CNT. *Appl. Catal., B* **2015**, *162*, 420−429.
(25) Domínguez, C.; Pérez-Alonso, F. J.; Al-Thabaiti, S. A.; Basahel, S. N.; Obaid, A. Y.; Alyoubi, A. O.; Gómez de la Fuente, J. L.; Rojas, S. Effect of N and S Co-doping of Multiwalled Carbon Nanotubes for the Oxygen Reduction. *Electrochim. Acta* **2015**, *157*, 158−165.

(26) Zhang, Y.; Fan, W.; Li, X.; Wang, W.-X.; Liu, S. Enhanced Removal of Free Radicals by Aqueous Hydrogen Nanobubbles and Their Role in Oxidative Stress. *Environ. Sci. Technol.* **2022**, *56* (21), 15096−15107.
(27) Yang, Z.; Gao, Y.; Zuo, L.; Long, C.; Yang, C.; Zhang, X. Tailoring Heteroatoms in Conjugated Microporous Polymers for Boosting Oxygen Electrochemical Reduction to Hydrogen Peroxide. *ACS Catal.* **2023**, *13* (7), 4790−4798.
(28) Shen, X.; Wang, Z.; Guo, H.; Lei, Z.; Liu, Z.; Wang, L. Solvent Engineering of Oxygen-Enriched Carbon Dots for Efficient Electrochemical Hydrogen Peroxide Production. *Small* **2023**, *19* (43), No. 2303156.
(29) Zhang, Y.; Zhao, Y.; Yermukhambetova, A.; Bakenov, Z.; Chen, P. Ternary sulfur/polyacrylonitrile/$Mg_{0.6}Ni_{0.4}O$ composite cathodes for high performance lithium/sulfur batteries. *J. Mater. Chem. A* **2013**, *1* (2), 295−301.
(30) Hu, B.; Wu, Y.; Wang, K.; Guo, H.; Lei, Z.; Liu, Z.; Wang, L. Gram-Scale Mechanochemical Synthesis of Atom-Layer MoS_2 Semiconductor Electrocatalyst via Functionalized Graphene Quantum Dots for Efficient Hydrogen Evolution. *Small* **2024**, *20* (2), No. 2305344.
(31) Xie, Y.; Zhao, J.; Le, Z.; Li, M.; Chen, J.; Gao, Y.; Huang, Y.; Qin, Y.; Zhong, R.; Zhou, D.; Ling, Y. Preparation and Electromagnetic Properties of Chitosan-Decorated Ferrite-Filled Multi-Walled Carbon Nanotubes/Polythiophene Composites. *Compos. Sci. Technol.* **2014**, *99*, 141−146.
(32) Xie, Y.; Hong, X.; Yu, C.; Li, M.; Huang, Y.; Gao, Y.; Zhao, J.; Yan, S.; Shi, L.; Zhang, K.; Lai, Q.; Ling, Y. Preparation and Magnetic Properties of Poly(3-octyl-thiophene) /$BaFe_{11.92}(LaNd)_{0.04}O_{19}$-Titanium Dioxide/Multiwalled Carbon Nanotubes Nanocomposites. *Compos. Sci. Technol.* **2013**, *77*, 8−13.
(33) Patil, I. M.; Reddy, V.; Lokanathan, M.; Kakade, B. Nitrogen and Sulphur Co-doped Multiwalled Carbon Nanotubes as an Efficient Electrocatalyst for Improved Oxygen Electroreduction. *Appl. Surf. Sci.* **2018**, *449*, 697−704.
(34) Dong, Y.; Feng, J.; Li, G. Transition Metal Ion-Induced High Electrocatalytic Performance of Conducting Polymer for Oxygen and Hydrogen Evolution Reactions. *Macromol. Chem. Phys.* **2017**, *218* (22), No. 1700359.
(35) Wang, Z.; Liu, L.; Bu, W.; Zheng, M.; Jin, N.; Zhang, K.; Xu, X.; Zhou, D.; Yang, B.; Sun, H. Carbon Dots Induce Epithelial-Mesenchymal Transition for Promoting Cutaneous Wound Healing via Activation of TGF-β/p38/Snail Pathway. *Adv. Funct. Mater.* **2020**, *30* (43), No. 2004886.
(36) Oka, K.; Tsujimura, O.; Suga, T.; Nishide, H.; Winther-Jensen, B. Light-Assisted Electrochemical Water-Splitting at Very Low Bias Voltage Using Metal-Free Polythiophene as Photocathode at High pH in a Full-Cell Setup. *Energy Environ. Sci.* **2018**, *11* (5), 1335−1342.
(37) Cosano, D.; Esquivel, D.; Puertas, A. J.; Romero-Salguero, F. J.; Jiménez-Sanchidrián, C.; Ruiz, J. R. Microstructural Analysis of 3D Hierarchical composites of Hydrotalcite-coated Silica Microspheres. *Microporous Mesoporous Mater.* **2021**, *323*, No. 111247.
(38) Shirotori, M.; Nishimura, S.; Ebitani, K. Fine-Crystallized LDHs Prepared with SiO_2 Spheres as Highly Active Solid Base Catalysts. *J. Mater. Chem. A* **2017**, *5* (15), 6947−6957.
(39) Zheng, H.; Yang, F.; Xiong, T.; Adekoya, D.; Huang, Y.; Balogun, M. S. J. T. Polypyrrole Hollow Microspheres with Boosted Hydrophilic Properties for Enhanced Hydrogen Evolution Water Dissociation Kinetics. *ACS Appl. Mater. Interfaces* **2020**, *12* (51), 57093−57101.
(40) Liu, Y.; Liu, S.; Xie, X.; Li, Z.; Wang, P.; Lu, B.; Liang, S.; Tang, Y.; Zhou, J. A Functionalized Separator Enables Dendrite-Free Zn Anode via Metal-Polydopamine Coordination Chemistry. *InfoMat* **2023**, *5* (3), No. e12374.
(41) Hu, C.; Chen, X.; Jin, J.; Han, Y.; Chen, S.; Ju, H.; Cai, J.; Qiu, Y.; Gao, C.; Wang, C.; Qi, Z.; Long, R.; Song, L.; Liu, Z.; Xiong, Y. Surface Plasmon Enabling Nitrogen Fixation in Pure Water through a Dissociative Mechanism under Mild Conditions. *J. Am. Chem. Soc.* **2019**, *141* (19), 7807−7814.
(42) Ballav, N.; Biswas, M. A Conducting Nanocomposite via Intercalative Polymerisation of Thiophene in Montmorillonite Clay. *Synth. Met.* **2004**, *142* (1), 309−315.
(43) Park, D. H.; Hong, Y. K.; Kim, M. S.; Cho, E. H.; Choi, W. J.; Kim, K. H.; Park, Q. H.; Kim, D.-C.; Song, H.; Kim, J.; Joo, J. Nanoscale Photoluminescence of Light-Emitting Poly (3-Methylthiophene) Nanotubes Hybridized with Au Nanoparticles. *Synth. Met.* **2010**, *160* (7), 604−608.
(44) Tu, W.; Xu, J.; Thompson, I. P.; Huang, W. E. Engineering Artificial Photosynthesis Based on Rhodopsin for CO_2 Fixation. *Nat. Commun.* **2023**, *14* (1), 8012.
(45) Selembo, P. A.; Merrill, M. D.; Logan, B. E. The Use of Stainless Steel and Nickel Alloys as Low-Cost Cathodes in Microbial Electrolysis Cells. *J. Power Sources* **2009**, *190* (2), 271−278.
(46) Schranck, A.; Doudrick, K. Effect of Reactor Configuration on the Kinetics and Nitrogen Byproduct Selectivity of Urea Electrolysis Using a Boron Doped Diamond Electrode. *Water Res.* **2020**, *168*, No. 115130.
(47) Dogutan, D. K.; Nocera, D. G. Artificial Photosynthesis at Efficiencies Greatly Exceeding That of Natural Photosynthesis. *Acc. Chem. Res.* **2019**, *52*, 3143.
(48) Cui, K.; Guo, K.; Carvajal-Arroyo, J. M.; Arends, J.; Rabaey, K. An Electrolytic Bubble Column with an External Hollow Fiber Membrane Gas−Liquid contactor for effective Microbial Electrosynthesis of Acetate from CO_2. *Chem. Eng. J.* **2023**, *471*, No. 144296.
(49) Li, Z.; Wang, L.; Li, Z.; Tian, R.; Lu, C. Efficient Bacteria Inactivation by Ligand-Induced Continuous Generation of Hydroxyl Radicals in Fenton-Like Reaction. *J. Hazard. Mater.* **2019**, *369*, 408−415.
(50) Cho, M.; Fortner, J. D.; Hughes, J. B.; Kim, J.-H. *Escherichia coli* Inactivation by Water-Soluble, Ozonated C_{60} Derivative: Kinetics and Mechanisms. *Environ. Sci. Technol.* **2009**, *43* (19), 7410−7415.
(51) Kang, F.; Qu, X.; Alvarez, P. J. J.; Zhu, D. Extracellular Saccharide-Mediated Reduction of Au^{3+} to Gold Nanoparticles: New Insights for Heavy Metals Biomineralization on Microbial Surfaces. *Environ. Sci. Technol.* **2017**, *51* (5), 2776−2785.
(52) Li, S.; Cao, Y.; Zhao, Z.; Zhang, Y. Regulating Secretion of Extracellular Polymeric Substances through Dosing Magnetite and Zerovalent Iron Nanoparticles To Affect Anaerobic Digestion Mode. *ACS Sustainable Chem. Eng.* **2019**, *7* (10), 9655−9662.
(53) Dong, J.; Zhang, Z.; Yu, Z.; Dai, X.; Xu, X.; Alvarez, P. J. J.; Zhu, L. Evolution and Functional Analysis of Extracellular Polymeric Substances during the Granulation of Aerobic Sludge Used to Treat p-Chloroaniline Wastewater. *Chem. Eng. J.* **2017**, *330*, 596−604.
(54) Xiao, Y.; Zhang, E.; Zhang, J.; Dai, Y.; Yang, Z.; Christensen, H. E. M.; Ulstrup, J.; Zhao, F. Extracellular Polymeric Substances are Transient Media for Microbial Extracellular Electron Transfer. *Sci. Adv.* **2017**, *3* (7), No. e1700623.
(55) Marsili, E.; Baron, D. B.; Shikhare, I. D.; Coursolle, D.; Gralnick, J. A.; Bond, D. R. *Shewanella* Secretes Flavins that Mediate Extracellular Electron Transfer. *Proc. Natl. Acad. Sci. U. S. A.* **2008**, *105* (10), 3968−3973.
(56) Wu, X.; Qiao, Y.; Shi, Z.; Tang, W.; Li, C. M. Hierarchically Porous N-Doped Carbon Nanotubes/Reduced Graphene Oxide Composite for Promoting Flavin-Based Interfacial Electron Transfer in Microbial Fuel Cells. *ACS Appl. Mater. Interfaces* **2018**, *10* (14), 11671−11677.
(57) Yang, M.; Xu, W.; Chen, Z.; Chen, M.; Zhang, X.; He, H.; Wu, Y.; Chen, X.; Zhang, T.; Yan, M.; Bai, J.; McAlinden, C.; Meek, K. M.; Yu, J.; Ding, S.; Gao, R.; Huang, J.; Zhou, X. Engineering Hibiscus-Like Riboflavin/ZIF-8 Microsphere Composites to Enhance Transepithelial Corneal Cross-Linking. *Adv. Mater.* **2022**, *34* (21), No. 2109865.
(58) Li, H.; Opgenorth, P. H.; Wernick, D. G.; Rogers, S.; Wu, T.-Y.; Higashide, W.; Malati, P.; Huo, Y.-X.; Cho, K. M.; Liao, J. C. Integrated Electromicrobial Conversion of CO_2 to Higher Alcohols. *Science* **2012**, *335* (6076), 1596−1596.
(59) Shen, J.; Xu, X.; Jiang, X.; Hua, C.; Zhang, L.; Sun, X.; Li, J.; Mu, Y.; Wang, L. Coupling of a Bioelectrochemical System for p-

https://doi.org/10.1021/cbe.4c00156
Chem Bio Eng. 2025, 2, 229−240

Nitrophenol Removal in an Upflow Anaerobic Sludge Blanket Reactor. *Water Res.* **2014**, *67*, 11−18.
(60) Jiang, X.; Shen, J.; Han, Y.; Lou, S.; Han, W.; Sun, X.; Li, J.; Mu, Y.; Wang, L. Efficient Nitro Reduction and Dechlorination of 2,4-dinitrochlorobenzene Through the Integration of Bioelectrochemical System into Upflow Anaerobic Sludge Blanket: A Comprehensive Study. *Water Res.* **2016**, *88*, 257−265.

https://doi.org/10.1021/cbe.4c00156
Chem Bio Eng. 2025, 2, 229−240